

# Inferring parameters for a lattice-free model of cell migration and proliferation using experimental data.

Alexander P. Browning<sup>a</sup>, Scott W. McCue<sup>a</sup>, Rachelle N. Binny<sup>b,c,d</sup>, Michael J. Plank<sup>b,d</sup>, Esha T. Shah<sup>e</sup>, Matthew J. Simpson<sup>a,\*</sup>

<sup>a</sup>*School of Mathematical Sciences, Queensland University of Technology (QUT), Brisbane, Australia.*

<sup>b</sup>*Landcare Research, Lincoln, Canterbury, New Zealand.*

<sup>c</sup>*Biomathematics Research Centre, University of Canterbury, Christchurch, New Zealand.*

<sup>d</sup>*Te Pūnaha Matatini, a New Zealand Centre of Research Excellence, New Zealand.*

<sup>e</sup>*Ghrelin Research Group, Translational Research Institute, QUT, 37 Kent St, Woolloongabba, Queensland, Australia.*

---

## Abstract

Collective cell spreading takes place in spatially continuous environments, yet it is often modelled using discrete lattice-based approaches. Here, we use data from a series of cell proliferation assays, with a prostate cancer cell line, to calibrate a spatially continuous individual based model (IBM) of collective cell migration and proliferation. The IBM explicitly accounts for crowding effects by modifying the rate of movement, direction of movement, and the rate of proliferation by accounting for pair-wise interactions. Taking a Bayesian approach we estimate the free parameters in the IBM using rejection sampling on three separate, independent experimental data sets. Since the posterior distributions from each experiment are similar, we perform simulations with parameters sampled from the combined distribution to explore the predictive power of the calibrated IBM by accurately forecasting the evolution of a fourth, experimental data set. Overall, we show how to calibrate a lattice-free IBM to experimental data, and our work highlights the importance of interactions between individuals. Despite great care taken to distribute cells as uniformly as possible experimentally, we find evidence of significant spatial clustering over short distances, suggesting that standard mean-field models could be inappropriate.

*Keywords:* individual based model, cell migration, model calibration, cell proliferation assay, approximate Bayesian computation

---

\*Corresponding author at: Mathematical Sciences, QUT, Brisbane, Australia. Tel.:+617 3138 5241; fax:+617 3138 2310

*Email address:* [matthew.simpson@qut.edu.au](mailto:matthew.simpson@qut.edu.au) ( Matthew J. Simpson)

## 1. Introduction

One of the most common *in vitro* cell biology experiments is called a *cell proliferation assay* (Bosco et al., 2015; Bourseguin et al., 2016; Browning et al., 2017). These assays are conducted by placing a monolayer of cells, at low density, on a two-dimensional substrate. Individual cells undergo proliferation and movement events, and the assay is monitored over time as the density of cells in the monolayer increases (Tremel et al., 2009). One approach to interpret a cell proliferation assay is to use a mathematical model (Warne et al. 2017). Calibrating the solution of a mathematical model to data from a cell proliferation assay can provide quantitative insight into the underlying mechanisms, by, for example, estimating the cell proliferation rate (Tremel et al., 2009; Sengers et al., 2007). A standard approach to modelling a cell proliferation assay is to use a mean-field model, which is equivalent to assuming that individuals within the population interact in proportion to the average population density and that there is no spatial structure, such as clustering (Tremel et al., 2009; Sengers et al., 2007; Maini et al., 2004b; Sarapata and de Pillis, 2014; Sherratt and Murray, 1990). More recently, increased computational power has meant that individual based models (IBMs) have been used to directly model the cell-level behaviour (Binny et al., 2016a; Frascoli et al., 2013; Johnston et al., 2014). IBMs are attractive for modelling biological phenomena because they can be used to represent properties of individual agents, such as cells, in the system of interest (Binny et al., 2016a,b; Frascoli et al., 2013; Peirce et al., 2004; Read et al., 2012; Treloar et al., 2013). Typical IBMs use a lattice, meaning that both the position of agents, and the direction of movement, are restricted (Codling et al., 2008). In contrast, lattice-free IBMs are more realistic because they enable agents to move in continuous space, in any direction. However, this extra freedom comes at the cost of higher computational requirements (Plank and Simpson, 2012).

In this work we consider a continuous-space, continuous-time IBM (Binny et al., 2016b). This IBM is well-suited to studying experimental data from a cell proliferation assay with PC-3 prostate cancer cells (Kaighn et al., 1979), as shown in Figure 1(a)-(d). The key mechanisms in the experiments include cell migration and cell proliferation, and we note that there is no cell death in the experiments on the time scale that we consider. Therefore, agents in the IBM are allowed to undergo both proliferation and movement events. Crowding effects that are often observed in two-dimensional

29 cell biology experiments (Cai et al., 2007) are explicitly incorporated into the IBM as the rates of  
30 proliferation and movement in the model are inhibited in regions of high agent density. In this study  
31 we specifically choose to work with the PC-3 cell line because these cells are known to be highly  
32 migratory, mesenchymal cells (Kaighn et al., 1979). This means that cell-to-cell adhesion is minimal  
33 for this cell line, and cells tend to migrate as individuals. We prefer to work with a continuous-space,  
34 lattice-free IBM as this framework gives us the freedom to identically replicate the initial location  
35 of all cells in the experimental data when we specify the initial condition in the IBM. In addition,  
36 lattice-free IBMs do not restrict the direction of movement like a lattice-based approach.

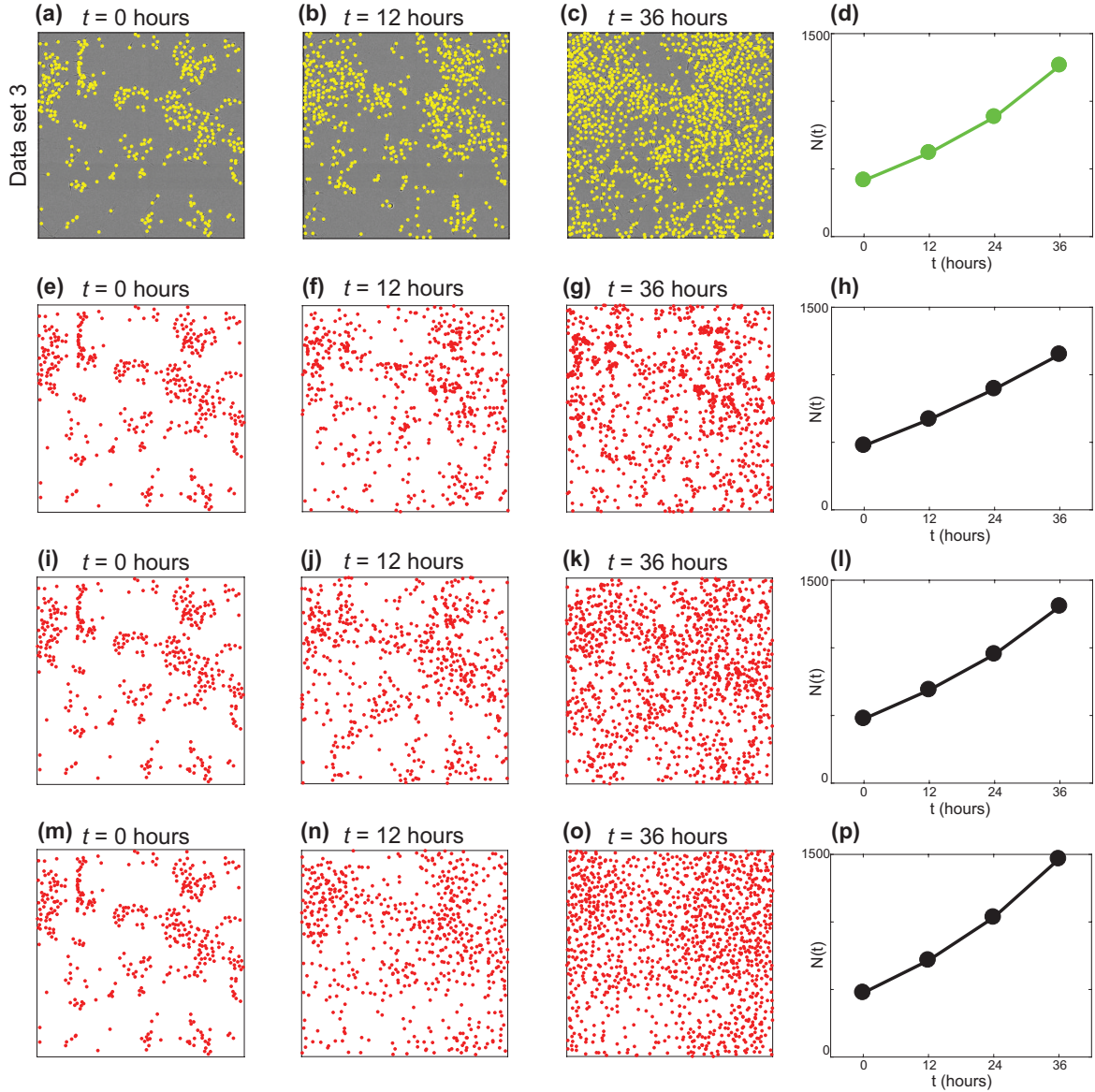


**Fig. 1:** (a)-(c) Experimental data set 3 at  $t = 0, 12$  and  $36$  hours. The position of each cell is identified with a yellow marker. The field of view is a square of length  $1440 \mu\text{m}$ . (d) Population size,  $N(t)$  for experimental data set 3. (e)-(h) One realisation of the IBM with  $\gamma_b = 0 \mu\text{m}$ , leading to an overly clustered distribution of agents. (i)-(l) One realisation of the IBM with  $\gamma_b = 6.0 \mu\text{m}$ , leading to a distribution of agents with similar clustering to the experimental data. (m)-(p) One realisation of the IBM with  $\gamma_b = 20 \mu\text{m}$ , leading to an overly segregated distribution of agents. All IBM simulations are initiated using the same distribution of agents as in (a), with  $m = 1.0$  /hour,  $p = 0.040$  /hour, and  $\sigma = 24 \mu\text{m}$ .

37 A key contribution of this study is to demonstrate how the IBM can be calibrated to experimen-  
38 tal data. In particular, we use approximate Bayesian computation (ABC) to infer the parameters  
39 in the IBM. Four sets of experimental images (Supplementary Material 1), each corresponding to  
40 an identically-prepared proliferation assay, are considered. The experiments are conducted over a  
41 duration of 36 hours, which is unusual because proliferation assays are typically conducted for no  
42 more than 24 hours (Browning et al., 2017). Data from the first three sets of experiments (Figure  
43 2) are used to calibrate the IBM and data from the fourth set of images is used to examine the  
44 predictive capability of the calibrated IBM. The IBM that we work with was presented very recently  
45 (Binny et al., 2016b). The description of the IBM by Binny et al. (2016b) involves a discussion of  
46 the mechanisms in the model and the derivation of a spatial moment continuum description (Binny  
47 et al., 2016b). [Our current work is the first time that experimental data has been used to provide](#)  
48 [parameter estimates for this new IBM.](#)

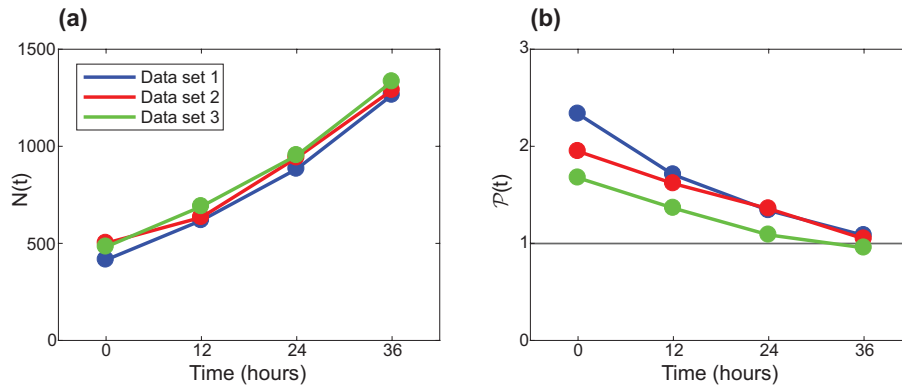


**Fig. 2:** Summary statistics for experimental data sets 1, 2 and 3, shown in blue, red and green, respectively. (a) Population size,  $N(t)$ . (b) Local measure of spatial structure,  $\mathcal{P}(t)$ , given by Equation 10. Unprocessed experimental data are given in Supplementary Material documents 1 and 2.

49 Taking a Bayesian approach, we assume that cell proliferation assays are stochastic processes,  
50 and model parameters are random variables, allowing us to update information about the model  
51 parameters using ABC (Collis et al., 2017; Tanaka et al., 2006). For this purpose we perform a large  
52 number of IBM simulations using parameters sampled from a prior distribution. Previous work, based  
53 on mean-field models, suggests that the proliferation rate and cell diffusivity for PC-3 cells is  $\lambda \approx 0.05$   
54 /hour and  $D \approx 175 \mu\text{m}^2/\text{hour}$ , respectively (Johnston et al., 2015). The prior distribution for the  
55 IBM parameters are taken to be uniform and to encompass these previous estimates. We generate  
56  $10^6$  realisations of the IBM using parameters sampled from the prior distribution, and accept the top  
57 1% of simulations that provide the best match to the experimental data. Our approach to connect  
58 the experimental data and the IBM is novel, we are unaware of any previous work that has used  
59 ABC to parameterise a lattice-free IBM of a cell proliferation assay. One possible reason why ABC  
60 methods are not routinely used to calibrate lattice-free models of cell migration and cell proliferation  
61 with crowding effects is because of high computational requirements (Fröhlich et al., 2016). For  
62 example, we find that the typical run time to simulate our experiments is approximately 2 seconds  
63 on a standard desktop machine using C++. This means that simulating  $10^6$  realisations for inference  
64 with three unknown parameters becomes challenging. All work presented here is simulated on a High  
65 Performance Computing cluster to manage these computational limitations (QUT High Performance  
66 Computing, 2017).

67 Applying the ABC algorithm to data from three sets of identically prepared experiments leads  
68 to three similar posterior distributions. This result provides confidence that the IBM is a realistic  
69 representation of the cell proliferation assays and leads us to produce a combined posterior distri-  
70 bution from which we use the mean to give point estimates of the model parameters. To provide  
71 further validation of the IBM, we use the combined posterior distribution and the IBM to make a  
72 prediction of the fourth experimental data set. Simulating the IBM with parameters sampled from  
73 the combined posterior distribution allows us to predict both the time evolution of the population  
74 size,  $N(t)$ , and a measure of the density of pairs of cells,  $\mathcal{P}(t)$ , which provides a measure of spatial  
75 structure. These results indicate that the *in silico* predictions are consistent with the experimental  
76 observations.

77 This manuscript is organised as follows. Sections 2.1-2.2 describe the experiments and the IBM,  
78 respectively. In Section 2.3 we explain how to apply the ABC algorithm to estimate the IBM param-  
79 eters. In Section 3 we present the marginal posterior distributions of the IBM parameters using data  
80 from the first three sets of experiments. The predictive power of the calibrated IBM is demonstrated  
81 by using the combined marginal posterior distributions to predict the fourth experimental data set.  
82 The predictive power of the calibrated IBM is compared with a stochastic analogue of the standard  
83 mean-field logistic equation (Murray, 2002). While both models can accurately predict  $N(t)$ , the lo-  
84 gistic equation provides no information about the spatial structure in the experimental data. Finally,  
85 in Section 4, we conclude and summarise opportunities for further research.

## 86 2. Material and methods

### 87 2.1. Experimental methods

88 We perform a series of proliferation assays using the IncuCyte ZOOM<sup>TM</sup> live cell imaging system  
89 (Essen BioScience, MI USA) (Jin et al., 2017). All experiments are performed using the PC-3 prostate  
90 cancer cell line (Kaighn et al., 1979). These cells, originally purchased from American Type Culture  
91 Collection (Manassas, VA, USA), are a gift from Lisa Chopin (April, 2016). Cells are propagated  
92 in RPMI 1640 medium (Life Technologies, Australia) with 10% foetal calf serum (Sigma-Aldrich,  
93 Australia), 100 U/mL penicillin, and 100  $\mu\text{g}/\text{mL}$  streptomycin (Life Technologies), in plastic tissue  
94 culture flasks (Corning Life Sciences, Asia Pacific). Cells are cultured in 5%  $\text{CO}_2$  and 95% air in a  
95 Panasonic incubator (VWR International) at 37 °C. Cells are regularly screened for *Mycoplasma*.

96 Approximately 8,000 cells are distributed in the wells of the tissue culture plate as uniformly  
97 as possible. After seeding, cells are grown overnight to allow for attachment and some subsequent  
98 growth. The plate is placed into the IncuCyte ZOOM<sup>TM</sup> apparatus, and images showing a field of view  
99 of size  $1440 \times 1440 \mu\text{m}$  are recorded every 12 hours for a total duration of 36 hours. Experimental  
100 images for experimental data set three is shown in Figure 1(a)-(c). Images from the other three  
101 data sets are provided in Supplementary Material 1. ImageJ is used to determine the approximate  
102 locations of individual cells in all images, this data is given in Supplementary Material 2. Summary  
103 statistics,  $N(t)$  and  $\mathcal{P}(t)$ , for the first three experimental data sets are given in 2(a)–(b).



104 *2.2. Mathematical model*

105 *2.2.1. Individual based model*

106 We consider an IBM describing the proliferation and movement of individual cells (Binny et al., 2016a,b).  
107 Since cell death is not observed in the experiments, the IBM does not include agent death. The IBM  
108 allows the net proliferation rate and the net movement rate of agents to depend on the spatial  
109 arrangement of other agents. To be consistent with previous experimental observations, the IBM  
110 incorporates a biased movement mechanism so that agents tend to move away from nearby crowded  
111 regions (Cai et al., 2007). We use the IBM to describe the dynamics of a population of agents on  
112 a square domain of length  $L = 1440 \mu\text{m}$  to match the field-of-view of the experimental data (Fig-  
113 ure 1(a)-(c)). Agents in the model are treated as a series of points which we may interpret as a  
114 population of uniformly-sized discs with diameter  $\sigma = 24 \mu\text{m}$  (Supplementary Material 1). Each  
115 agent has location  $\mathbf{x}_n = (x_1, x_2)$ , for  $n = 1, \dots, N(t)$ . Since the field-of-view of each image is much  
116 smaller than the size of the well in the tissue culture plate, we apply periodic boundary conditions  
117 (Jin et. al., 2017).

118 Proliferation and movement events occur according to a Poisson process over time (Binny et al., 2016b).  
119 The  $n$ th agent is associated with neighbourhood-dependent rates,  $P_n \geq 0$  and  $M_n \geq 0$ , of prolifer-  
120 ation and movement, respectively. These rates consist of intrinsic components,  $p > 0$  and  $m > 0$ ,  
121 respectively. Crowding effects are introduced by reducing the intrinsic rates by a contribution from  
122 other neighbouring agents. These crowding effects are calculated using a kernel,  $w^{(\cdot)}(r)$ , that depends  
123 on the separation distance,  $r \geq 0$ , so that

$$P_n = \max \left( 0, p - \sum_{i \neq n}^{N(t)} w^{(p)}(r) \right), \quad (1)$$

$$M_n = \max \left( 0, m - \sum_{i \neq n}^{N(t)} w^{(m)}(r) \right). \quad (2)$$

124 Following Binny et al.,(2016), we specify the kernels to be Gaussian with width corresponding to the

125 cell diameter,  $\sigma$ , giving

$$w^{(p)}(r) = \gamma_p \exp\left(-\frac{r^2}{2\sigma^2}\right), \quad (3)$$

$$w^{(m)}(r) = \gamma_m \exp\left(-\frac{r^2}{2\sigma^2}\right). \quad (4)$$

126 Here,  $\gamma_p$  is the value of  $w^{(p)}(0)$  and  $\gamma_m$  is the value of  $w^{(m)}(0)$ . These parameters provide a measure  
127 of the strength of crowding effects on agent proliferation and movement, respectively. The kernels,  
128  $w^{(p)}(r)$  and  $w^{(m)}(r)$ , ensure that the interactions between pairs of agents separated by more than  
129 roughly 2-3 cell diameters lead to a negligible contribution. For computational efficiency, we truncate  
130 the Gaussian kernels so that  $w^{(p)}(r) = w^{(m)}(r) = 0$ , for  $r \geq 3\sigma$  (Law et al., 2003).

131 To reduce the number of unknown parameters in the IBM, we specify  $\gamma_p$  and  $\gamma_m$  by invoking an  
132 assumption about the maximum packing density of the population. Here we suppose that the net  
133 proliferation and net movement rates reduce to zero when the agents are packed at the maximum  
134 possible density, which is a hexagonal packing (Figure 3(a)). For interactions felt between the nearest  
135 neighbours only (Figure 3(b)), we obtain

$$\gamma_p = \frac{p}{6} \exp\left(\frac{1}{2}\right), \quad (5)$$

$$\gamma_m = \frac{m}{6} \exp\left(\frac{1}{2}\right), \quad (6)$$

136 which effectively specifies a relationship between  $\gamma_p$  and  $p$ , and between  $\gamma_m$  and  $m$ . Note that this  
137 assumption does not preclude a formation of agents in which some pairs have a separation of less  
138 than  $\sigma$  and densities greater than hexagonal packing, which can occur by chance.

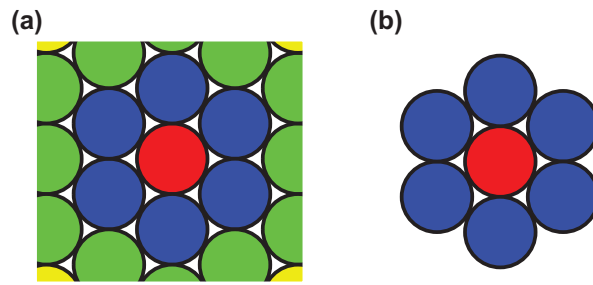


**Fig. 3:** (a) Hexagonal packing of uniformly sized discs. The focal agent (red) is surrounded by six nearest neighbouring agents (blue), and twelve next nearest neighbouring agents (green). (b) Hexagonal packing around a focal agent (red) showing the six nearest neighbours only.

139 When an agent at  $\mathbf{x}_n$  proliferates, the location of the daughter agent is selected by sampling  
140 from a bivariate normal distribution with mean  $\mathbf{x}_n$  and variance  $\sigma^2$  (Binny et al., 2016b). Since  
141 mesenchymal cells in two-dimensional cell culture are known to move with a directional movement  
142 bias away from regions of high density (Cai et al., 2007), we allow the model to incorporate a bias  
143 so that the preferred direction of movement is in the direction of decreasing agent density. For  
144 simplicity, the distance that each agent steps is taken to be a constant, equal to the cell diameter,  $\sigma$   
145 (Plank and Simpson, 2012).

146 To choose the movement direction, we use a crowding surface,  $B(\mathbf{x})$ , to measure the local crowd-  
147 edness at location  $\mathbf{x}$ , given by

$$B(\mathbf{x}) = \sum_{i=1}^{N(t)} w^{(b)}(\|\mathbf{x} - \mathbf{x}_i\|). \quad (7)$$

148 The crowding surface is the sum of contributions from every agent, given by a bias kernel,  $w^{(b)}(r)$ .  
149 The contributions depend on the distance between  $\mathbf{x}$  and the location of the  $i$ th agent,  $\mathbf{x}_i$ , given by  
150  $r = \|\mathbf{x} - \mathbf{x}_i\|$ . Again, we choose  $w^{(b)}$  to be Gaussian, with width equal to the cell diameter, and  
151 repulsive strength,  $\gamma_b \geq 0$ , so that

$$w^{(b)}(r) = \gamma_b \exp\left(-\frac{r^2}{2\sigma^2}\right), \quad (8)$$

152 where  $\gamma_b$  is value of  $w^{(b)}(0)$ , and has dimensions of length. Note that  $B(\mathbf{x})$  is an increasing function  
153 of local density, and approaches zero as the local density decreases. A typical crowding surface is  
154 shown in Figure 4(b) for the arrangement of agents in Figure 4(a).

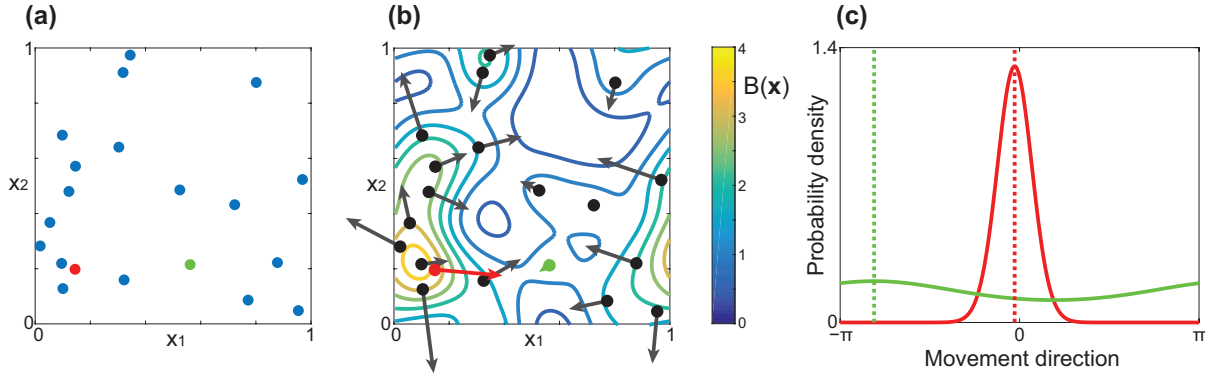


**Fig. 4:** (a) Example distribution of agents on a  $1 \times 1$  periodic domain. (b) Level curves of the corresponding crowding surface,  $B(\mathbf{x})$ , for this arrangement of agents. The arrows show the preferred direction of movement,  $\mathbf{B}_n$ . To illustrate how the direction of movement is chosen, (c) shows the probability density of the von Mises distribution for the red and green agents highlighted in (a) and (b). The preferred direction,  $\arg(\mathbf{B}_n)$ , is shown as dotted vertical lines for both agents. The red agent is in a crowded region so  $\|\mathbf{B}_n\|$  is large, meaning that the agent is likely to move in the preferred direction  $\arg(\mathbf{B}_n)$ . The green agent is in a low density region and  $\|\mathbf{B}_n\|$  is small, meaning that the bias is very weak and the agent's direction of movement is almost uniformly distributed. To illustrate the effects of the crowding surface as clearly as possible, we set  $\gamma_b = 1$ ,  $\sigma = 0.1$ ,  $L = 1$  in this schematic figure to draw attention to the gradient of the crowding surface.

155 To determine the direction of movement we use the shape of  $B(\mathbf{x})$  to specify the bias, or preferred  
 156 direction, of agent  $n$ ,  $\mathbf{B}_n$ , given by

$$\mathbf{B}_n = -\nabla B(\mathbf{x}_n), \quad (9)$$

157 which gives the magnitude and direction of steepest descent. Results in Figure 4(b) show  $\mathbf{B}_n$  for  
 158 the arrangement of agents in Figure 4(a). To determine the direction of movement, we consider  
 159 the magnitude and direction of  $\mathbf{B}_n$ , and sample the actual movement direction from a von Mises  
 160 distribution,  $\text{von Mises}(\arg(\mathbf{B}_n), \|\mathbf{B}_n\|)$  (Binny et al., 2016b; Forbes et al., 2011). Therefore, agents  
 161 are always most likely to move in the direction of  $\mathbf{B}_n$ , however as  $\|\mathbf{B}_n\| \rightarrow 0$ , the preferred direction  
 162 becomes uniformly distributed.

163 To illustrate how the direction of movement is chosen, we show, in Figure 4(b), the bias vector  
 164 for each agent,  $\mathbf{B}_n$ . Note that  $\mathbf{B}_n$  does not specify the movement step length, and the direction of  $\mathbf{B}_n$   
 165 does not necessarily specify the actual direction. Rather,  $\arg(\mathbf{B}_n)$  specifies the preferred direction.  
 166 To illustrate this property, we highlight two agents in Figure 4(a). The red agent is located on a  
 167 relatively steep part of the crowding surface, so  $\|\mathbf{B}_n\|$  is large. The green agent is located on a  
 168 relatively flat part of the crowding surface, so  $\|\mathbf{B}_n\|$  is close to zero. Figure 4(c) shows the von Mises  
 169 distributions for the red and green agent. Comparing these movement distributions confirms that  
 170 the crowded red agent is more likely to move in the direction of  $\mathbf{B}_n$ . The bias is weak for the green  
 171 agent, so the direction of movement is almost uniformly distributed since  $\|\mathbf{B}_n\|$  is smaller.

172 IBM simulations are performed using the Gillespie algorithm (Gillespie, 1977). To initialise each  
 173 simulation we specify the initial number and initial location of agents to match to the experimental  
 174 images at  $t = 0$  hours (Supplementary Material 1) for experimental data sets 1, 2, 3 and 4. In all  
 175 simulations we set  $\sigma = 24 \mu\text{m}$  and  $L = 1440 \mu\text{m}$ . The remaining three parameters,  $m$ ,  $p$  and  $\gamma_b$ , are  
 176 varied with the aim of producing posterior distributions using a Bayesian framework.

177 If  $\gamma_m = \gamma_b = 0$ , and the variance of the dispersal distribution is large, the IBM corresponds to  
 178 logistic growth (Binny et al., 2016b, Browning et al. 2017). Under these simplified conditions, a  
 179 uniformly distributed initial population of agents will grow, at rate  $p$ , to eventually reach a uniformly  
 180 distributed maximum average density of  $p/(2\pi\gamma_p\sigma_p^2)$ . We do not consider this case here as our initial  
 181 distribution of cells in the experiments is clustered, and so the logistic growth model is, strictly

182 speaking, not valid (Binny et al., 2016b).

### 183 2.2.2. Summary statistics

184 To match the IBM simulations with the experimental data we use properties that are related  
185 to the first two spatial moments (Law et al., 2003). The first spatial moment, the average density,  
186 is characterised by the number of agents in the population,  $N(t)$ . The second spatial moment  
187 characterises how agents are spatially distributed, and is often reported in terms of a pair correlation  
188 function (Binny et al., 2016a,b; Law et al., 2003). In the Supplementary Material 1 document we  
189 present the pair correlation function for all four experimental data sets. These results show that  
190 we have a fairly typical pair correlation function that contains, at most, one maximum (Binder and  
191 Simpson, 2013). Therefore, instead of using all details contained in the pair correlation function, we  
192 use a simplified measure of spatial structure. We consider a local measure of pair density within a  
193 distance of  $R$   $\mu\text{m}$ , given by

$$\mathcal{P}(t) = \frac{L^2 \sum_{i=1}^{N(t)} \sum_{\substack{j=1 \\ j \neq i}}^{N(t)} \mathbb{I}_{\|\mathbf{x}_i - \mathbf{x}_j\| \leq R}}{N(t)^2 \pi R^2}, \quad (10)$$

194 where  $\mathbb{I}$  is an indicator function so that the double sum in Equation 10 gives twice the number of  
195 distinct pairs within a distance  $R$ . For all results presented in the main document we set  $R = 50$   $\mu\text{m}$ .  
196 Therefore,  $\mathcal{P}(t)$  is the ratio of the number of pairs of agents, separated by a distance of less than  
197  $50$   $\mu\text{m}$ , to the expected number of pairs of agents separated by a distance of less than  $50$   $\mu\text{m}$ , if  
198 the agents were randomly distributed. This means that,  $\mathcal{P}(t) = 1$  corresponds to randomly placed  
199 agents;  $\mathcal{P}(t) > 1$  corresponds to a locally clustered distribution; and,  $\mathcal{P}(t) < 1$  corresponds to a  
200 locally segregated distribution.

201 To ensure that our choice of setting  $R = 50$   $\mu\text{m}$  is adequate, we also repeat some results with  
202  $R = 100$   $\mu\text{m}$ . This exercise leads to very similar posterior distributions, confirming that working  
203 with  $R = 50$   $\mu\text{m}$  is sufficient (Supplementary Material 1).

### 204 2.3. Approximate Bayesian computation

205 We consider  $m, p$  and  $\gamma_b$  as random variables, and the uncertainty in these parameters is updated  
206 using observed data (Collis et al., 2017; Tanaka et al., 2006). To keep the description of the inference

207 algorithm succinct, we refer to the unknown parameters as  $\Theta = \langle m, p, \gamma_b \rangle$ .

208 In the absence of any experimental observations, information about  $\Theta$  is characterised by specified  
 209 prior distributions. The prior distributions are chosen to be uniform on an interval that is wide enough  
 210 to encompass previous estimates of  $m$  and  $p$  (Johnston et al., 2015). To characterise the prior for  
 211  $\gamma_b$ , we note that this parameter is related to a length scale over which bias interactions are felt.  
 212 Preliminary results (not shown) use a prior in the interval  $0 \leq \gamma_b \leq 20 \mu\text{m}$  and suggest that a narrow  
 213 prior in the interval  $0 \leq \gamma_b \leq 10 \mu\text{m}$  is appropriate. In summary, our prior distributions are uniform  
 214 and independent, given by

$$\pi(m) = \text{U}(0, 10) \text{ /hour}, \quad (11)$$

$$\pi(p) = \text{U}(0, 0.1) \text{ /hour}, \quad (12)$$

$$\pi(\gamma_b) = \text{U}(0, 10) \mu\text{m}. \quad (13)$$

215 We always summarise data,  $\mathbf{X}$ , with a lower-dimensional summary statistic,  $S$ . Data and summary  
 216 statistics from the experimental images are denoted  $\mathbf{X}_{\text{obs}}$  and  $S_{\text{obs}}$ , respectively. Similarly, data  
 217 and summary statistics from IBM simulations are denoted  $\mathbf{X}_{\text{sim}}$  and  $S_{\text{sim}}$ , respectively. Information  
 218 from the prior is updated by the likelihood of the observations,  $\pi(S_{\text{obs}}|\Theta)$ , to produce posterior  
 219 distributions,  $\pi(\Theta|S_{\text{obs}})$ . We employ the most fundamental ABC algorithm, known as ABC rejection  
 220 (Liepe et al., 2014; Tanaka et al., 2006), to sample from the approximate posterior distribution. The  
 221 approximate posterior distributions are denoted  $\pi_u(\Theta|S_{\text{obs}})$ .

222 In this work we use a summary statistic that is a combination of  $N(t)$  and  $\mathcal{P}(t)$  at equally spaced  
 223 time intervals. A discrepancy measure,  $\rho(S_{\text{obs}}, S_{\text{sim}})$ , is used to assess the closeness of  $S_{\text{obs}}$  and  $S_{\text{sim}}$ ,

$$\rho(S_{\text{obs}}, S_{\text{sim}}) = \sum_t \left( \frac{[N_{\text{sim}}(t) - N_{\text{obs}}(t)]^2}{N_{\text{obs}}(t)^2} + \frac{[\mathcal{P}_{\text{sim}}(t) - \mathcal{P}_{\text{obs}}(t)]^2}{\mathcal{P}_{\text{obs}}(t)^2} \right), \quad (14)$$

224 Algorithm 1 is used to obtain  $10^6 u$  samples,  $\{\Theta_i\}_{i=1}^{10^6 u}$ , from the approximate joint posterior distri-  
 225 bution,  $\pi_u(\Theta|S_{\text{obs}})$ , for each data set. Here,  $u \ll 1$  is the accepted proportion of samples.

226 To present marginal posterior samples, we use a kernel density estimate to form smooth, approx-  
 227 imate marginal posterior distributions, for each parameter, and each data set using the `ksdensity`



---

**Algorithm 1** ABC rejection sampling algorithm to obtain  $10^6 u$  samples from the approximate posterior distribution,  $\pi_u(\Theta | S_{\text{obs}})$ .

---

- 1: Set  $\sigma = 24 \mu\text{m}$ ,  $L = 1440 \mu\text{m}$ , and set  $\mathbf{x}_n$  to match experimental data  $\mathbf{X}_{\text{obs}}$  at  $t = 0$ .
  - 2: Draw parameter samples from the prior  $\Theta_i \sim \pi(\Theta)$ .
  - 3: Simulate cell proliferation assay with  $\Theta_i$  and  $t \leq 36$  hours.
  - 4: Record summary statistic  $S_{\text{sim}_i} = \{N_{\text{sim}}(t), \mathcal{P}(t)\}_t$ , where  $t = 12, 24$  and  $36$  hours.
  - 5: Compute the discrepancy measure  $\epsilon_i = \rho(S_{\text{obs}}, S_{\text{sim}_i})$ , given in Equation 14.
  - 6: Repeat steps 2-5 until  $10^6$  samples  $\{\Theta_i, \epsilon_i\}_{i=1}^{10^6}$  are simulated.
  - 7: Order  $\{\Theta_i, \epsilon_i\}_{i=1}^{10^6}$  by  $\epsilon_i$  such that  $\epsilon_1 < \epsilon_2 < \dots$
  - 8: Retain the first 1% ( $u = 0.01$ ) of prior samples  $\Theta_i$ , as posterior samples,  $\{\Theta_i\}_{i=1}^{10^6 u}$ .
- 

228 function in MATLAB (Mathworks, 2017). Point estimates of parameters are always given as the  
 229 mean of the posterior distribution, and always presented to two significant figures.

230 *2.3.1. Sampling from the combined posterior distribution*

231 Samples from the posterior distributions for each experimental data set are given in Supplemen-  
 232 tary Material 1. Kernel density estimates for the marginal posterior distributions for each exper-  
 233 imental data set are given in Figure 5. Visually, the posterior distributions for each experimental  
 234 data set appear to be similar, therefore we are motivated to form a combined posterior distribution,  
 235  $\pi_u(\Theta | \{S_{\text{obs}}^{(k)}\}_{k=1}^3)$ , where  $S_{\text{obs}}^{(k)}$  is the summary statistic from the  $k$ th experimental data set. We use  
 236 ABC rejection to sample from the combined posterior distribution according to Algorithm 2. That  
 237 is, Algorithm 2 is designed to sample the combined posterior distribution by retaining the top 1% of  
 238 parameter combinations that provide the best fit to all three experimental data sets.

---

**Algorithm 2** ABC rejection sampling algorithm to obtain  $10^6 u$  samples from the approximate combined posterior distribution,  $\pi_u(\Theta | \{S_{\text{obs}}^{(k)}\}_{k=1}^3)$ .

---

- 1: Set  $\sigma = 24 \mu\text{m}$ ,  $L = 1440 \mu\text{m}$ .
  - 2: Draw parameter samples from the prior  $\Theta_i \sim \pi(\Theta)$ .
  - 3: For experimental data sets  $k = 1, 2$  and  $3$ :
    - 3.1: Set  $\mathbf{x}_n$  to match experimental data set  $k$ ,  $\mathbf{X}_{\text{obs}}^{(k)}$  at  $t = 0$ .
    - 3.2: Simulate cell proliferation assay with  $\Theta_i$  and  $t \leq 36$  hours.
    - 3.3: Record summary statistic  $S_{\text{sim}_i}^{(k)} = \{N_{\text{sim}}(t), \mathcal{P}(t)\}_t$ , where  $t = 12, 24$  and  $36$  hours.
  - 4: Compute the discrepancy measure  $\epsilon_i = \sum_{k=1}^3 \rho(S_{\text{obs}}^{(k)}, S_{\text{sim}_i}^{(k)})$ , where  $\rho$  is given in Equation 14.
  - 5: Repeat steps 2-4 until  $10^6$  samples  $\{\Theta_i, \epsilon_i\}_{i=1}^{10^6}$  are simulated.
  - 6: Order  $\{\Theta_i, \epsilon_i\}_{i=1}^{10^6}$  by  $\epsilon_i$  such that  $\epsilon_1 < \epsilon_2 < \dots$
  - 7: Retain the first 1% ( $u = 0.01$ ) of prior samples  $\Theta_i$ , as posterior samples,  $\{\Theta_i\}_{i=1}^{10^6 u}$ .
-

239 *2.3.2. Predicting experimental data set 4 using the combined posterior distribution*

240 To test the predictive power of the calibrated IBM, we use  $10^4$  parameter samples from the  
241 combined posterior distribution and simulate the IBM initialised with the actual initial arrangement  
242 of cells in data set 4 at  $t = 0$ . For each parameter combination  $S_{\text{sim}}$  is recorded at 12 hour intervals,  
243 and used to construct distributions of  $N(t)$  and  $\mathcal{P}(t)$ . These distributions are represented as box  
244 plots and compared with summary statistics from experimental data set 4.

245 *2.3.3. Calibrating the standard mean-field logistic model to the experimental data*

246 To illustrate the importance of considering individual level details in the IBM, we also calibrate  
247 the logistic growth model to experimental data sets 1, 2 and 3. The logistic growth model describes  
248 the IBM when spatial structure is neglected (Law et al., 2003; Binny et al., 2016b). The logistic  
249 growth model is given by

$$\frac{dN(t)}{dt} = \lambda N(t) \left( 1 - \frac{N(t)}{N_{\text{max}}} \right), \quad (15)$$

250 where  $\lambda$  is the cell proliferation rate and  $N_{\text{max}}$  is the maximum number of agents. To find estimates  
251 of  $\lambda$  and  $N_{\text{max}}$  to best match our experimental data we simulate the stochastic logistic model using  
252 the Gillespie algorithm (Gillespie, 1977; Fröhlich et. al., 2016). Proliferation events are treated as  
253 a Poisson process, with the rate given by the right hand side of Equation 15. Details of the ABC  
254 rejection algorithm used to estimate  $\lambda$  and  $N_{\text{max}}$  are given in Supplementary Material 1.

255 **3. Results and discussion**

256 To qualitatively illustrate the importance of spatial structure we show, in rows 2-4 of Figure 1,  
257 snapshots from the IBM with different choices of parameters. In each case the IBM simulations  
258 evolve from the initial condition specified in Figure 1(a). Results in the right-most column of Figure  
259 1 compare the evolution of  $N(t)$  and we see that the parameter combination in the second row  
260 underestimates  $N(t)$ , the parameter combination in the fourth row overestimates  $N(t)$ , and the  
261 parameter combination in the third row produces a reasonable match to the experimental data. A  
262 visual comparison of the spatial arrangement of agents in rows 2-4 of Figure 1 suggests that these  
263 different parameter combinations may lead to different spatial structures. This illustration of how  
264 the IBM results vary with the choice of parameters motivates us to use ABC rejection to estimate the

265 joint distribution of the parameters. To do this we will use summary statistics from three identically  
266 prepared, independent sets of experiments. The summary statistics for these experiments,  $N(t)$  and  
267  $\mathcal{P}(t)$ , are summarised in Figure 2, and tabulated in Supplementary Material 1.

268 The approximate marginal posterior distributions for  $m$ ,  $p$  and  $\gamma_b$  are shown in Figure 5(a)-(c),  
269 respectively, for experimental data sets 1, 2 and 3. There are several points of interest to note.  
270 In each case, the posterior support is well within the interior of the prior support, suggesting that  
271 our choice of priors is appropriate. An interesting feature of the marginal posterior distributions  
272 for all parameters is that there is significant overlap for each independent experimental data set.  
273 There is some variation in the mean between experimental data sets, for each parameter, which  
274 could arise as a consequence of some other variation among experiments, or under the assumption  
275 that cell proliferation assays are stochastic processes. The combined marginal posterior distributions  
276 are superimposed, and the mean is given by 1.0 /hour, 0.040 /hour and 6.0  $\mu\text{m}$  for  $m$ ,  $p$  and  $\gamma_b$ ,  
277 respectively. These point estimates of  $p$  and  $m$  give a cell doubling time of  $\ln(2)/p \approx 17$  hours, and a  
278 cell diffusivity of approximately 150  $\mu\text{m}^2/\text{hour}$ , which are typical values for PC-3 cells at low density  
279 (Johnston et al., 2015). All results in the main document correspond to retaining the top 1% of  
280 samples ( $u = 0.01$ ) and additional results (Supplementary Material 1) confirm that the results are  
281 relatively insensitive to this choice.

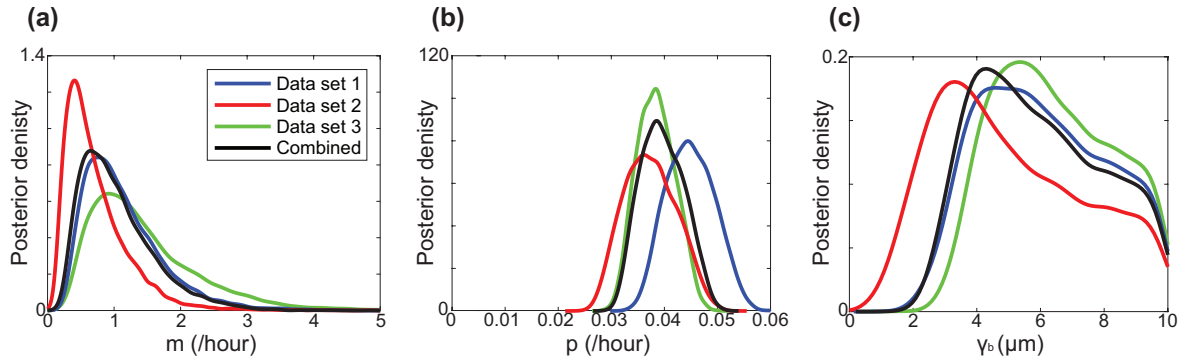


**Fig. 5:** (a)-(c) Kernel-density estimates of the approximate marginal posterior distributions for each data set, for parameters  $m$ ,  $p$  and  $\gamma_b$ , respectively, with  $u = 0.01$ . The combined posterior distribution (black) is superimposed. The point estimates from the combined posterior distribution are  $m = 1.0$  /hour,  $p = 0.040$  /hour and  $\gamma_b = 6.0$   $\mu\text{m}$ . All distributions are scaled so that the area under the curve is unity.

282 To assess the predictive power of the calibrated IBM, we attempt to predict the time evolution  
283 of a separate, independently collected data set, experimental data set 4, as shown in Figure 6(a)-(d).  
284 We use the mean of the combined posterior distribution and the initial arrangement of agents in  
285 experimental data set 4 to produce a typical prediction in Figure 6(e)-(h). Visual comparison of the  
286 experimental data and the IBM prediction suggests that the IBM predicts a similar number of agents,  
287 and a similar spatial structure, with some short range clustering present. To quantify our results,  
288 we compare the evolution of  $N(t)$  in Figure 6(i) which reveals an excellent match. Furthermore, we  
289 predict the evolution of  $\mathcal{P}(t)$  in Figure 6(j) confirming similar trends.

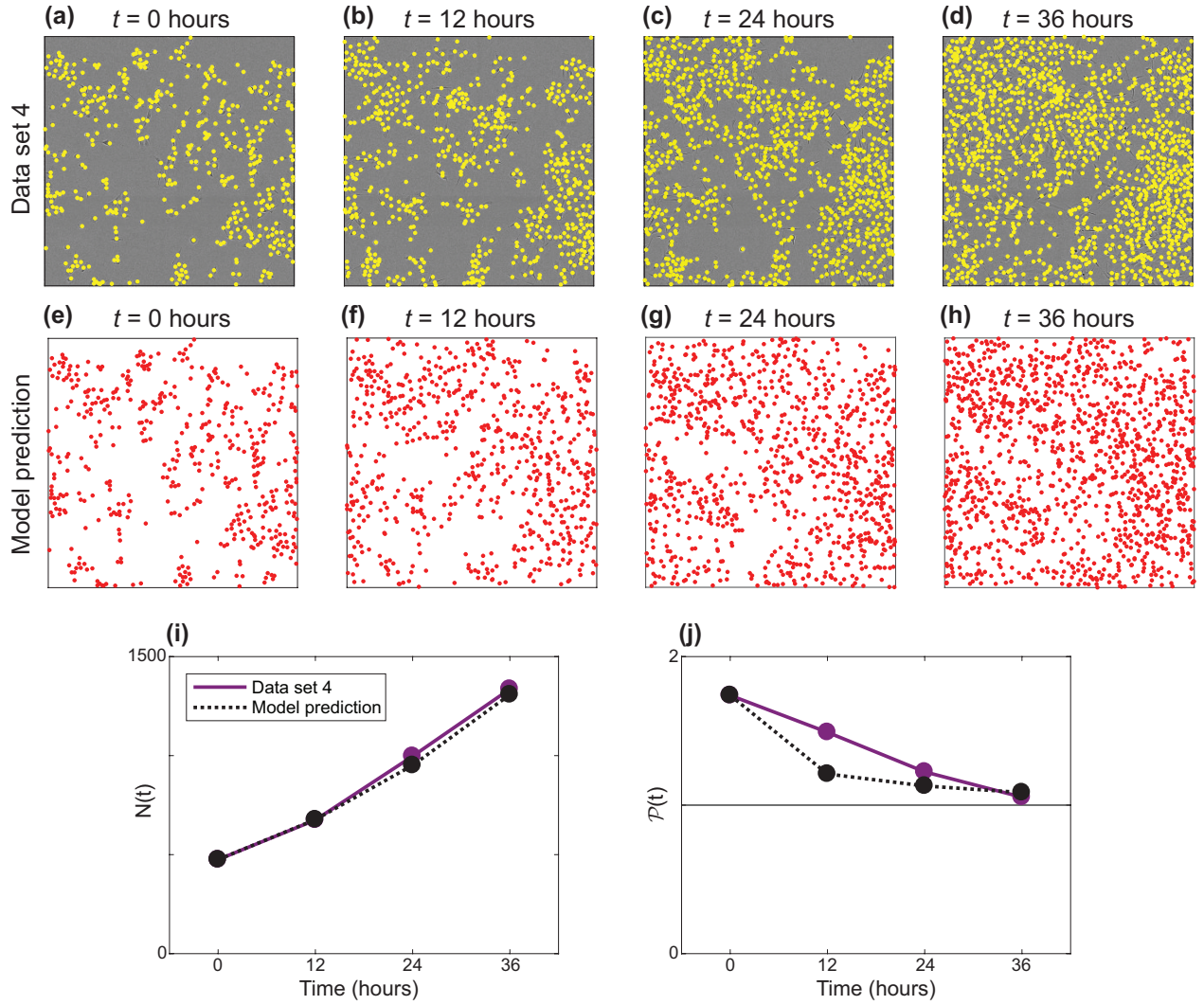


**Fig. 6:** (a)-(d) Experimental images for data set 4. The position of each cell is identified with a yellow marker. The field of view is a square of length  $1440 \mu\text{m}$ . (e)-(h) One realisation of the IBM with parameters corresponding to the posterior mean:  $m = 1.0$  /hour,  $p = 0.040$  /hour and  $\gamma_b = 6.0 \mu\text{m}$ , with the same initial arrangement of agents as in (a). (i)  $N(t)$  for the experimental data (purple) and the IBM prediction (dashed black). (j)  $\mathcal{P}(t)$  for the experimental data (purple) and the IBM prediction (dashed black). The quality of fit is measured by the coefficient of determination,  $R_N^2 = 0.99$ ,  $R_P^2 = 0.67$ .

290 In addition to examining a single, typical realisation of the calibrated model, we now examine a  
291 suite of realisations of the calibrated IBM, and compare results with experimental data set 4. The  
292 suite of IBM realisations is obtained by sampling from the joint posterior distribution. Results in  
293 Figure 7(a) compare  $N(t)$  from experimental data set 4 with distributions of  $N(t)$  from the suite of  
294 IBM simulations, showing an excellent match. The spread of the distributions of  $N(t)$  increases with  
295 time, which is expected. Results in Figure 7(b) compare the evolution of  $\mathcal{P}(t)$  from experimental  
296 data set 4 with distributions of  $\mathcal{P}(t)$  from the suite of IBM simulations, showing the predicted  
297 distributions of  $\mathcal{P}(t)$  overlap with the experimental data. Overall, the quality of the match between  
298 the prediction and the experimental data is high, as the prediction captures both qualitative and  
299 quantitative features of the data.

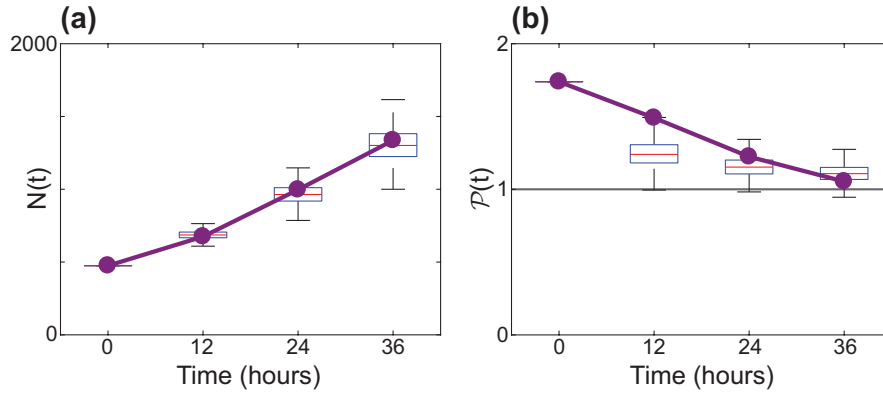


**Fig. 7:** Predictive distributions for  $N(t)$  and  $\mathcal{P}(t)$ , respectively, generated using the IBM.  $10^4$  parameter samples are taken from the combined posterior distribution, and a model realisation produced for each sample, initiated as in Figure 6(a). Box plots show the distribution of  $N(t)$  and  $\mathcal{P}(t)$  across these realisations in (a) and (b), respectively. The quality of fit is measured by the coefficient of determination, where the discrepancy is taken to be between the mean of each boxplot and the observed data,  $R_N^2 = 1.00$ ,  $R_P^2 = 0.75$ .



300 We now use ABC rejection to form combined posterior distributions of the parameters in the  
301 standard logistic growth model, Equation 15,  $\lambda$  and  $N_{\max}$ . Results are shown in Figure 8(a)–(b).  
302 The point estimates of the combined posterior distributions are  $\lambda = 0.037$  /hour and  $N_{\max} = 3600$ .  
303 This estimate leads to a doubling time of approximately 19 hours, which is slightly longer than the  
304 doubling time predicted using the calibrated IBM. We then examine a suite of solutions of Equation  
305 15, where we sample from the combined posterior distribution for  $\lambda$  and  $N_{\max}$ . The predicted  
306 distribution of  $N(t)$  is compared with experimental data set 4 in Figure 8(c), revealing an excellent  
307 match.

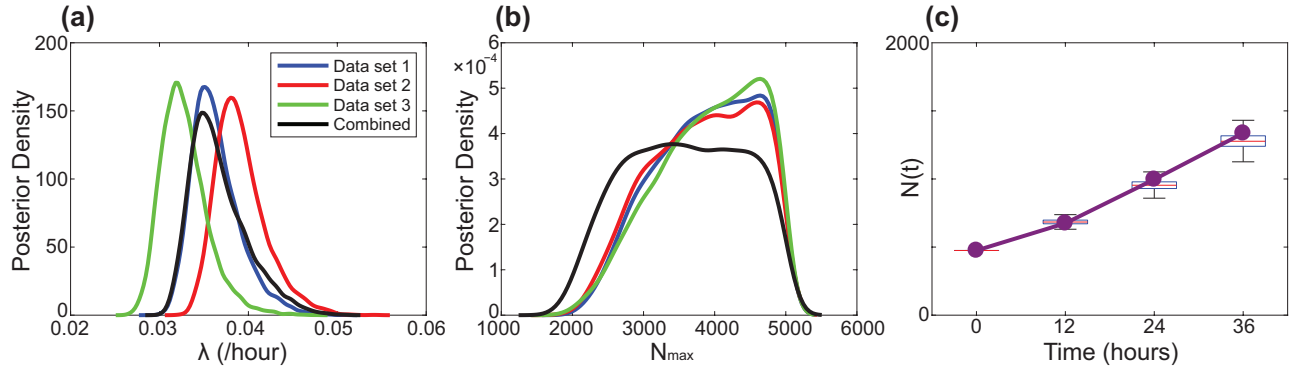


**Fig. 8:** (a)- (b) Kernel-density estimates of the marginal posterior distributions are shown for each data set, for parameters in the stochastic logistic model, Equation 15,  $\lambda$  and  $N_{\max}$  in (a) and (b), respectively. The combined posterior distribution (black) is superimposed. The point estimates are  $\lambda = 0.037$  /hour and  $N_{\max} = 3600$ . All marginal distributions are scaled to an area of unity. (c) A predictive distribution for  $N(t)$ , generated from the stochastic logistic model, Equation 15.  $10^4$  parameter samples are taken from the combined posterior distribution, and a model realisation produced for each sample. Boxplots show the distribution of  $N(t)$  across these realisations. The procedure for sampling from the combined posterior distribution for the stochastic logistic model, and the procedure for solving the stochastic logistic model, are outlined in Supplementary Material 1. The quality of fit is measured by the coefficient of determination, where the discrepancy is taken to be between the mean of each boxplot and the observed data,  $R_N^2 = 0.98$ .

308 Therefore, while both calibrated models provide good predictions for the observed evolution of  
309  $N(t)$ , the IBM offers additional insights relating to spatial structure in the cell population, while the  
310 logistic model does not provide this level of information. The differences in the way that the logistic  
311 model and the IBM treat interactions between individuals could explain why the calibration process  
312 leads to different estimates of the proliferation rate. These differences suggest that the interactions  
313 between individuals appear to be relevant for our experimental data.

#### 314 4. Conclusions

315 In this work we explore how to connect a spatially continuous IBM of cell migration and cell prolif-  
316 eration to novel data from a cell proliferation assay. Previous work parameterising IBM models of cell  
317 migration and cell proliferation to experimental data using ABC have been restricted to lattice-based  
318 IBMs (Johnston et al., 2014). This is partly because ABC methods require large numbers of IBM  
319 simulations, and lattice-based IBMs are far less computationally expensive than lattice-free IBMs  
320 (Plank and Simpson, 2012). We find it is preferable to work with a lattice-free IBM when dealing  
321 with experimental data as a lattice-based IBM requires approximations when mapping the distribu-  
322 tion of cells from experimental images to a lattice (Johnston et al., 2014; Johnston et al., 2016). This  
323 mapping can be problematic. For example, if multiple cells in an experimental image are equally  
324 close to one lattice site, *ad hoc* assumptions have to be introduced about how to arrange those cells  
325 on the lattice without any overlap. These issues are circumvented using a lattice-free method.

326 To help overcome the computational cost of using ABC with a lattice-free IBM, we introduce  
327 several realistic, simplifying assumptions. The IBM originally presented by Binny et al. (2016b)  
328 involves 12 free parameters, which is a relatively large number for standard inference techniques  
329 (Schnoerr et al. 2016). The model is simplified by noting that our experiments do not involve  
330 cell death, and specifying the width of the interaction kernels to be constant, given by the cell  
331 diameter. Another simplification is given by assuming that crowding effects reduce the proliferation  
332 and movement rates to zero when the agents are packed at the maximum hexagonal packing density.  
333 This leads to a simplified model with three free parameters:  $m$ ,  $p$  and  $\gamma_b$ . Using ABC rejection,  
334 we arrive at posterior distributions for these parameters for three independent experimental data  
335 sets. The marginal posterior distributions for the three parameters are similar, leading us to form a

336 combined posterior distribution. The point estimates from the combined posterior distributions for  $m$   
337 and  $p$  are consistent with previous parameter estimates (Johnston et al., 2015) and the point estimate  
338 for  $\gamma_b$  is consistent with previous observations that mesenchymal cells in this kind of two-dimensional  
339 experiment tend to move away from regions of high cell density (Cai et al., 2007).

340 In the field of mathematical biology, questions about how much detail to include in a mathe-  
341 matical model, and what kind of mathematical model is preferable for understanding a particular  
342 biological process are often settled in an *ad hoc* manner, as discussed by Maclaren et al. (2015). Our  
343 approach in this work is to use a mathematical model that incorporates just the key mechanisms,  
344 with an appropriate number of unknown parameters. Other approaches are possible, such as using  
345 much more complicated mathematical models that describe additional mechanisms such as: (i) de-  
346 tailed information about the cell cycle in individual cells (Fletcher et al., 2012); (ii) concepts of leader  
347 and follower cells (Kabla, 2012); (iii) explicitly coupling cell migration and cell proliferation to the  
348 availability of nutrients and growth factors (Tang et al., 2014); or (iv) including mechanical forces  
349 between cells (Stichel et al., 2017). However, we do not include these kinds of detailed mechanisms  
350 because our experimental data does not suggest that these mechanisms are relevant to our situa-  
351 tion. Furthermore, it is not always clear that using a more complicated mathematical model, with  
352 additional mechanisms and additional unknown parameters, necessarily leads to improved biological  
353 insight. In fact, simply incorporating additional mechanisms and parameters into the mathematical  
354 model often leads to a situation where multiple parameter combinations lead to equivalent predic-  
355 tions which limits the usefulness of the mathematical model (Simpson et al., 2006). In this study,  
356 our approach is to be guided by experimental data and our ability to infer the parameters in a math-  
357 ematical model based on realistic amounts of experimental data (Maclaren et al. 2015). In particular  
358 we use three experimental data sets to calibrate the IBM, and an additional data set to separately  
359 examine the predictive capability of the calibrated IBM. We find that the process of calibrating the  
360 IBM leads to well defined posterior distributions of the model parameters, and that the calibrated  
361 IBM produces a reasonable match to the experimental data. The process of calibrating the IBM,  
362 and then separately testing the predictive capability of the calibrated IBM, provides some confidence  
363 that the level of model complexity is appropriate for our purposes.

364 An interesting feature of all experimental data at early time, when the cell density is relatively  
365 low, is that  $\mathcal{P}(t)$  suggests that the cells are clustered at short intervals, and that this clustering  
366 becomes less pronounced with time. This observation is very different to the way that previous  
367 theoretical studies have viewed the role of spatial structure. For example, previous simulation-  
368 based studies assume that some initial random spatial arrangement of cells can lead to clustering  
369 at later times (Baker and Simpson, 2010). In contrast, our experimental data suggests it could be  
370 more realistic to consider that the spatial structure is imposed by the initial arrangement of cells.  
371 Moreover, since all of our experimental data involves some degree of spatial clustering, our work  
372 highlights the importance of using appropriate models to provide a realistic representation of key  
373 phenomena. Almost all continuum models of collective behaviour in cell populations take the form of  
374 ordinary differential equations and partial differential equations that implicitly invoke a mean-field  
375 assumption (Tremel et al., 2009; Sengers et al., 2007; Maini et al., 2004b; Sarapata and de Pillis,  
376 2014; Sherratt and Murray, 1990). Such assumptions ignore the role of spatial structure. While pair-  
377 wise models that avoid mean-field assumptions are routine in some fields, such as disease spreading  
378 (Sharkey et al., 2006; Sharkey, 2008) and ecology (Law et al., 2003), models that explicitly account  
379 for spatial structure are far less common for collective cell behaviour.

380 Using our parameter estimates, the continuum spatial moment description could be used to inter-  
381 pret experimental data sets with larger numbers of cells (Binny et al., 2016b), such as experimental  
382 images showing a wider field-of-view, or experiments initiated with a higher density of cells. Our  
383 approach to estimate the parameters in the model is to work with the IBM since this allows us more  
384 flexibility in connecting with the experimental data, such as choosing the initial locations of the  
385 agents in the IBM to precisely match the initial locations of cells in the experimental images.

386 There are many ways that our study could be extended. For example, here we choose a summary  
387 statistic encoding information about the first two spatial moments. However, other summary statis-  
388 tics may provide different insight, and it could be of interest to explore the effect of this choice. For  
389 example, here we describe the spatial structure over a relatively short interval, approximately  $2\sigma$ . It  
390 could be of interest to repeat our analysis using the entire pair correlation function, accounting for  
391 spatial structure at all distances. However, here we take a simpler approach and we provide evidence

392 that our results are insensitive to our measure of spatial structure as we obtain similar results when  
393 we consider spatial structure over larger distances. Another limitation of our work is that the IBM,  
394 which explicitly accounts for interactions between agents, can be computationally expensive to simu-  
395 late. This limitation can be particularly problematic for computational inference and severely limits  
396 the number of parameters that can be dealt with by taking a purely individual-based approach.  
397 One promising way of overcoming this difficulty is to make use of more theoretical ways to treat  
398 interactions between individuals in an IBM, and to perform inference using some kind of stochastic  
399 continuum description, such as the recent work by Schnoerr et al. (2016; 2017).

## 400 5. Acknowledgements

401 This work is supported by the Australian Research Council (DP140100249, DP170100474) and  
402 the Royal Society of New Zealand Marsden Fund (11-UOC-005). Computational resources provided  
403 by the High Performance Computing and Research Support Group at QUT are appreciated. We  
404 thank David Warne for technical advice. We also thank the two anonymous referees for their helpful  
405 comments.

## 406 6. References

- 407 [1] Baker RE, Simpson MJ. 2010. Correcting mean-field approximations for birth-death-movement  
408 processes. *Phys Rev E* **82**, 041905.
- 409 [2] Binder, BJ, Simpson, MJ. 2013. Quantifying spatial structure in experimental observations and  
410 agent-based simulations using pair-correlation functions. *Phys Rev E* **88**, 022705.
- 411 [3] Binny RN, Haridas P, James A, Law R, Simpson MJ, Plank MJ. 2016a. Spatial structure arising  
412 from neighbour-dependent bias in collective cell movement. *PeerJ* **4**, e1689.
- 413 [4] Binny RN, James A, Plank MJ. 2016b. Collective cell behaviour with neighbour-dependent pro-  
414 liferation, death and directional bias. *Bull Math Biol* **78**, 2277–2301.
- 415 [5] Bosco DB, Kenworthy R, Zorio DAR, Sang QXA. 2015. Human mesenchymal stem cells are  
416 resistant to paclitaxel by adopting a non-proliferative fibroblastic state. *PLoS One* **10**, e0128511.

- 417 [6] Bourseguin J, Bonet C, Renaud E, Pandiani C, Boncompagni M, Giuliano S, Pawlikowska P,  
418 Karmous-Benailly H, Ballotti R, Rosselli F, Bertolotto C. 2016. FANCD2 functions as a critical  
419 factor downstream of MiTF to maintain the proliferation and survival of melanoma cells. *Sci Rep*  
420 **6**, 36539.
- 421 [7] Browning AP, McCue SW, Simpson MJ. 2017. A Bayesian computational approach to explore  
422 the optimal duration of a cell proliferation assay. *Bull Math Biol* **10**, 1888-1906.
- 423 [8] Cai AQ, Landman KA, Hughes BD. 2007. Multi-scale modeling of a wound-healing cell migration  
424 assay. *J Theor Biol* **245**, 576–594.
- 425 [9] Codling EA, Plank MJ, Benhamou S. 2008. Random walk models in biology. *J R Soc Interface*  
426 **5**, 813–834.
- 427 [10] Collis J, Connor AJ, Paczkowski M, Kannan P, Pitt-Francis J, Byrne HM, Hubbard ME. 2017.  
428 Bayesian calibration, validation and uncertainty quantification for predictive modelling of tumour  
429 growth: a tutorial. *Bull Math Biol* **79**, 939–974.
- 430 [11] Fletcher AG, Breward CJW, Chapman SJ. 2012. Mathematical modelling of monoclonal con-  
431 version in the colonic crypt. *J Theor Biol* **300**, 118–133.
- 432 [12] Forbes C, Evans M, Hastings N, Peacock B. 2011. *Statistical distributions*. 4th ed. John Wiley  
433 & Sons, New Jersey.
- 434 [13] Frascoli F, Hughes BD, Zaman MH, Landman KA. 2013. A computational model for collective  
435 cellular motion in three dimensions: general framework and case study for cell pair dynamics. *PLoS*  
436 *ONE* **8**, e59249.
- 437 [14] Fröhlich, F, Thomas, P, Kazeroonian, A, Theis, FJ, Grima, R, Hasenauer, J, 2016. Inference  
438 for stochastic chemical kinetics using moment equations and system size expansion. *PLoS Comput*  
439 *Biol* **12**, e1005030.
- 440 [15] Gillespie DT. 1977. Exact stochastic simulation of coupled chemical reactions. *J Phys Chem* **81**,  
441 2340–2361.

- 442 [16] QUT High Performance Computing. 2017 [https://www.student.qut.edu.au/technology/research-](https://www.student.qut.edu.au/technology/research-computing/high-performance-computing)  
443 [computing/high-performance-computing](https://www.student.qut.edu.au/technology/research-computing/high-performance-computing) Accessed: October 2017.
- 444 [17] Kabla AJ. 2012. Collective cell migration: leadership, invasion and segregation. *J R Soc Interface*  
445 **9**, 20120448.
- 446 [18] Jin W, Shah ET, Penington CJ, McCue SW, Maini PK, Simpson MJ. 2017. Logistic proliferation  
447 of cells in scratch assays is delayed. *Bull Math Biol* **79**, 1028–1050.
- 448 [19] Johnston ST, Simpson MJ, McElwain DLS, Binder BJ, Ross JV. 2014. Interpreting scratch  
449 assays using pair density dynamics and approximate Bayesian computation. *Open Biol* **4**, 140097.
- 450 [20] Johnston ST, Shah ET, Chopin LK, McElwain DLS, Simpson MJ. 2015. Estimating cell diffu-  
451 sivity and cell proliferation rate by interpreting IncuCyte ZOOM™ assay data using the Fisher-  
452 Kolmogorov model. *BMC Syst Biol* **9**, 38.
- 453 [21] Johnston ST, Ross JV, Binder BJ, McElwain DLS, Haridas P, Simpson MJ. 2016. Quantifying  
454 the effect of experimental design choices for in vitro scratch assays. *J Theor Biol* **400**, 19–31.
- 455 [22] Kaighn ME, Narayan KS, Ohnuki Y, Lechner JF, Jones LW. 1979. Establishment and charac-  
456 terization of a human prostatic carcinoma cell line (PC-3). *Invest Urol* **17**, 16–23.
- 457 [23] Law R, Murrell DJ, Dieckmann U. 2003. Population growth in space and time: Spatial logistic  
458 equations. *Ecology* **84**, 252–262.
- 459 [24] Liepe J, Kirk P, Filippi S, Toni T, Barnes CP, Stumpf MPH. 2014. A framework for parameter  
460 estimation and model selection from experimental data in systems biology using approximate  
461 Bayesian computation. *Nat Protoc* **9**, 439–456.
- 462 [25] Maclaren OJ, Byrne HM, Fletcher AG, Maini PK. 2015. Models, measurement and inference in  
463 epithelial tissue dynamics. *Math Biosci Eng* **12**, 1321.
- 464 [26] Maini PK, McElwain DLS, Leavesley DI. 2004. Traveling wave model to interpret a wound-  
465 healing cell migration assay for human peritoneal mesothelial cells. *Tissue Eng* **10**, 475–482.



- 466 [27] Mathworks. 2017. Kernel smoothing function estimate for univariate and bivariate data.  
467 <http://www.mathworks.com/help/stats/ksdensity.html>. Accessed: October 2017.
- 468 [28] Murray JD. 2002. *Mathematical Biology*. Springer, Berlin.
- 469 [29] Peirce SM, Van Gieson EJ, Skalak TC. 2004. Multicellular simulation predicts microvascular  
470 patterning and in silico tissue assembly. *FASEB J* **18**, 731–733.
- 471 [30] Plank MJ, Simpson MJ. 2012. Models of collective cell behaviour with crowding effects: com-  
472 paring lattice-based and lattice-free approaches. *J R Soc Interface* **9**, 2983-2996.
- 473 [31] Read M, Andrews PS, Timmis J, Kumar V. 2012. Techniques for grounding agent-based sim-  
474 ulations in the real domain: a case study in experimental autoimmune encephalomyelitis. *Math*  
475 *Comp Model Dyn* **18**, 67–86.
- 476 [32] Sarapata EA, de Pillis LG. 2014. A comparison and catalog of intrinsic tumor growth models.  
477 *Bull Math Biol* **76**, 2010–2024.
- 478 [33] Sengers BG, Please CP, Oreffo ROC. 2007. Experimental characterization and computational  
479 modelling of two-dimensional cell spreading for skeletal regeneration. *J R Soc Interface* **4**, 1107.
- 480 [34] Sharkey KJ, Fernandez C, Morgan KL, Peeler E, Thrush M, Turnbull JF, Bowers RG. 2006.  
481 Pair-level approximations to the spatio-temporal dynamics of epidemics on asymmetric contact  
482 networks. *J Math Biol* **53**, 61–85.
- 483 [35] Sharkey KJ. 2008. Deterministic epidemiological models at the individual level. *J Math Biol* **57**,  
484 311–331.
- 485 [36] Sherratt JA, Murray JD. 1990. Models of epidermal wound healing. *P Roy Soc Lond B* **241**, 29.
- 486 [37] Schnoerr, D, Grima, R, Sanguinetti, G. 2016. Cox process representation and inference for  
487 stochastic reaction-diffusion processes. *Nat Commun* **7**, 11729.
- 488 [38] Schnoerr, D, Sanguinetti, G, Grima, R. 2017. Approximation and inference methods for stochas-  
489 tic biochemical kineticsa tutorial review. *J Phys A* **50**, 093001.

- 490 [39] Simpson MJ, Landman KA, Hughes BD, Newgreen DF. 2006. Looking inside an invasion wave  
491 of cells using continuum models: Proliferation is the key. *J Theor Biol* **243**, 343–360.
- 492 [40] Stichel D, Middleton AM, Müller BF, Depner S, Klingmüller U, Breuhahn K, Matthäus F.  
493 2017. An individual-based model for collective cancer cell migration explains speed dynamics and  
494 phenotype variability in response to growth factors. *NPJ Syst Biol Appl* **3**, 5.
- 495 [41] Tanaka MM, Francis AR, Luciani F, Sisson SA. 2006. Using approximate Bayesian computation  
496 to estimate tuberculosis transmission parameters from genotype data. *Genetics* **173**, 1511–1520.
- 497 [42] Tang L, van de Ven AL, Guo D, Andasari V, Cristini V, Li KC, Zhou X. 2014. Computational  
498 modeling of 3D tumor growth and angiogenesis for chemotherapy evaluation. *PLoS One* **9**, e83962.
- 499 [43] Treloar KK, Simpson MJ, Haridas P, Manton KJ, Leavesley DI, McElwain DLS, Baker RE. 2013.  
500 Multiple types of data are required to identify the mechanisms influencing the spatial expansion  
501 of melanoma cell colonies. *BMC Syst Biol* **7**, 137.
- 502 [44] Tremel A, Cai A, Tirtaatmadja N, Hughes BD, Stevens GW, Landman KA, O’Connor AJ. 2009.  
503 Cell migration and proliferation during monolayer formation and wound healing. *Chem Eng Sci*  
504 **64**, 247–253.
- 505 [45] Warne DJ, Baker RE, Simpson MJ. 2017. Optimal quantification of contact inhibition in cell  
506 populations. In press *Biophysical Journal* <https://doi.org/10.1016/j.bpj.2017.09.016>